JOURNAL OF GEOPHYSICAL RESEARCH, VOL. 92, NO. A10, PAGES 11,059-11,073, OCTOBER 1, 1987

ONE-DIMENSIONAL HYBRID SIMULATIONS OF BOUNDARY LAYER PROCESSES IN THE AMPTE SOLAR WIND LITHIUM RELEASES

S. C. Chapman and S. J. Schwartz

Astronomy Unit, School of Mathematical Sciences
Queen Mary College, London

Abstract. As part of the Active Magnetospheric Particle Tracer Explorers (AMPTE) mission, releases of ~ 10^{25} atoms of lithium, and later barium, were made in the solar wind and magnetosheath. Initial photoionization produced a release plasma of sufficient densities that a diamagnetic cavity was seen to form at the release center, disrupting the ambient field and flow over a localized region (approximately tens of kilometers for Li, approximately hundreds of kilometers for Ba). Since the gyroradii of both the oncoming solar wind protons and the release ions were either greater than or of the order of the scale size of this perturbation while the electron gyroradii remained small, a hybrid description, where the ions are treated as particles, and the electrons as a charge-neutralizing fluid, is appropriate. Here we present the results of one-dimensional simulations for lithium using a hybrid description in order to investigate the process of momentum transfer between the two ion species that occurs locally over the boundary layer which forms between them. We find that a well-defined field and plasma structure evolves in which the bulk of the lithium ions are moved en masse by a "snowplough" type process, those remaining either being accelerated to higher speeds to produce "taillike" structures or remaining upstream to form part of the snowplough momentum balance. Field and ion density structures found in the simulations are in good gross agreement with observations. We also obtain an analytical estimate of the snowplough speed which is in good agreement with that obtained computationally. When set in the context of the three-dimensional release geometry, features resolved by our one-dimensional simulation are found to have clear parallels in the AMPTE data.

1. Introduction

On September 11 and 20, 1984, as part of the Active Magnetospheric Particle Tracer Explorers (AMPTE) mission [Krimigis et al. 1982] two releases of ~ 3×10^{25} atoms of neutral lithium were made from the German Ion Release Module (IRM) spacecraft when it and the United Kingdom subsatellite (UKS) were located in the solar wind, upstream of Earth's bow shock. The UKS-IRM separation at these times was ~ 30-35 km.

A subsequent solar wind release of a similar number of photoionizing barium neutrals took place on the dawn flank of the magnetosphere on December 27, 1984, and in this case the spacecraft separation was larger, ~ 170 km. All the releases produced similar perturbations in the field and flow structure, although the heavier barium with a much shorter photoionization time (~ 30 s compared with ~ 1 hour) gave rise to a higher initial ion density and longer-lived dramatic disturbance.

The magnetic field signatures seen by both spacecraft for these releases are reported by Lühr et al. [1986a, b].

Paper number 7A9036.
0148-0227/87/007A-9036$05.00

In all cases the release plasma density is sufficiently high to suppress the field to zero at the IRM, for ~ 6 s for lithium and ~ 80 s for barium. This diamagnetic cavity is not seen to extend to the UKS, giving an upper limit on the scale size of the interaction region. If we consider the gyroscales of the ions involved, the applicability of a hybrid description, treating ions as particles and electrons as fluid, becomes clear. The Larmor radii of lithium and barium which have been "picked up" as test ions in the ambient solar wind flow are ~ $\frac{1}{2}$ R_E and ~ 10 R_E, respectively, shrinking by a factor of ~ 6-10 in the enhanced magnetic fields observed during these events. The corresponding gyroperiods in the ambient field are ~ 1 min for lithium and ~ 20 min for barium. For solar wind protons the relevant scales may be of the order of the release scales (a 5-eV proton has ~ 31 km gyroradius in the ambient fields and a gyroperiod of ~ 6 s), although we shall see that during the interaction between the protons and the release plasma these scales can vary significantly. The electrons, on the other hand, with gyroradii in general of a few hundred meters and gyroperiods of a few milliseconds, can as far as the ion interaction is concerned be viably treated as a massless, charge-neutralizing fluid, and it is the transfer of momentum between the two ion species that will be addressed here.

Previous work has concentrated on discussing the global three-dimensional aspects of the release physics, such as field line draping, wake formation behind the obstacle, and multifluid flow patterns from both analytical [Haerendel et al., 1986; Cheng, 1987, Papadopoulos and Lui, 1986] and numerical [Lui et al., 1986; Brecht and Thomas, 1987] points of view. One of the principal aims of most of these descriptions was to explain the initial motion of the barium release ion cloud, which was deduced from optical observations to be transverse to the direction of the oncoming ambient flow.

Here, instead of beginning with this global approach we shall concentrate on resolving the detailed momentum transfer processes occurring locally, over the dynamic boundary that evolves between the release ions, with their associated field free region, and the oncoming solar wind proton flow. It has already been demonstrated [Chapman and Dunlop, 1986] that an investigation of local, as well as global, considerations is essential in understanding the coupling of the release plasma to the ambient flow. We shall then see that the resolved structure to be discussed here also has implications for the global dynamics of the release ion - solar wind interaction.

We hence begin this detailed investigation by conducting the simplest possible numerical experiment. The one-dimensional simulation presented here is intended primarily to reveal the early time processes which take place locally, across the dynamic boundary between the release plasma and the oncoming solar wind. In the next section we first introduce the details of the simulation and discuss the validity of the assumptions that it implies for this particular study. In section 3 we present the results, which illustrate the local acceleration mechanisms

for the release ions. Finally, in section 4 these results and their implications are briefly discussed in the light of the gross features of the observations.

2. Details of the Simulation

2.1 Simulation Model

The simulation discussed here was performed with a one-dimensional hybrid code, in which all the ion species are represented by particles, while the electrons are represented by a single massless, charge-neutralizing fluid. The validity of these approximations is addressed in the appendix. All vector components are retained in three directions, being allowed only to vary in a single ($\hat{x}$) direction. Full details of the numerical schemes used are given by Winske and Leroy [1984]. Here we briefly outline the calculation, for future reference. First, the ion motion is given by their single-particle equations of motion, from initial values of the electromagnetic fields:

$$\frac{m_i}{q_i}\frac{d\underline{v}_i}{dt} = \underline{E} + \underline{v}_i \wedge \underline{B} - \eta \underline{J} \qquad (1)$$

where $-\eta\underline{J}$ represents a resistive force imposed by the electrons, the resistivity η being kept constant here. The assumption of quasi-neutrality, along with the continuity equation, then implies $J_x = 0$, while $\nabla \cdot \underline{B} = 0$ constrains B_x to be constant. Expressing the transverse components of $\underline{B}$ through the vector potential $\underline{A}$ then, neglecting the displacement current, gives

$$-\frac{1}{\mu_0}\frac{\partial^2 A_{y,z}}{\partial x^2} = J_{y,z} \qquad (2)$$

The transverse component of the massless electron fluid momentum equation is just

$$\eta J_{y,z} = E_{y,z} + (\underline{v}_e \wedge \underline{B})_{y,z} \qquad (3)$$

which includes the frictional coupling term $\eta\underline{J}$. Given that

$$E_{y,z} = -\frac{\partial A_{y,z}}{\partial t} \qquad E_x = -\frac{\partial \rho}{\partial x} \qquad (4)$$

once the ion motion has been integrated over a time step and their bulk parameters found, (2) and (3) may be solved for the transverse components of the vector potential and electron velocity. The massless electron fluid energy equation

$$\left[\frac{\partial}{\partial t} + V_{ex}\frac{\partial}{\partial x}\right] P_e = -\gamma P_e \frac{\partial V_{ex}}{\partial x} + (\gamma - 1)\eta J^2 \qquad (5)$$

($\gamma = 5/3$) can then be solved for the electron fluid pressure. This finally allows us to solve for the $\hat{x}$ electric field, from the $\hat{x}$ component of the massless electron fluid momentum equation:

$$E_x = -(\underline{v}_e \wedge \underline{B})_x - \frac{1}{ne}\frac{\partial P_e}{\partial x} \qquad (6)$$

The ions are then moved again using (1) to continue the calculation.

Solving coupled equations (2) and (3) for the transverse components of the vector potential requires suitable boundary conditions on $A_{y,z}$. Similarly, the boundary conditions on the electron energy equation (5) must be specified. Our simulations use constant electron pressure and magnetic field at both boundaries.

2.2 Initial Conditions

The one-dimensional simulation box used for this study represents 250 km along the $\hat{x}$ direction (the direction of variation) and is divided into 400 cells, giving an effective resolution of $\sim 3\Delta x \simeq 2$ km (due to the finite differencing required to obtain the fields at each time step). In comparison, $c/\omega_{pe} \sim 2.2$ km in the ambient solar wind, decreasing in higher-density regions where the release plasma is present, so that our choice of resolution should allow all larger-scale structures to be well resolved. The results to be discussed here are found to be independent of the grid size, other than detailed features being eventually lost due to lack of resolution as Δx is increased substantially. The solar wind initially pervades the box, at a density $n_{sw} = 5$ cm^{-3}, mean speed $V_{sw} = 500$ km s^{-1}, and temperature $T_e = T_p = 5$ eV (i.e., $M_{Asw} \sim 5$, $\beta_p \sim 0.1$). For simplicity the release ion density has been chosen here to vary as $1 + \tanh((x-x_0)/L)$, falling asymptotically to zero at the upstream boundary of our one-dimensional box and rising to 100 cm^{-3} at the downstream boundary. The midpoint in the density, x_0, here is at $x = 180$ km, and the half thickness, $L = 20$ km, is chosen to illustrate the behavior of release ions located both inside and outside the cavity. The downstream lithium ion density used here is approximately a factor of 10 smaller than that observed by the IRM when it passes through the edge of the diamagnetic cavity [Gurnett et al., 1986a], but we shall see that it still gives a sufficient contrast with the ambient solar wind parameters to produce well-defined behavior which is characteristic of the observed interaction. In this initial study we have not represented changes in the release ion density due to photoionization. Instead the lithium is all created at $t = 0$, moving upstream as an essentially cold beam with $v_{Li} = 2$ km s^{-1}, further ions being introduced at the downstream boundary as necessary to keep the release ion density there constant. This is a reasonable first approximation since the time scale of the simulation results given here (~ 1 s) is much smaller than the lithium photoionization time scale, although we shall see that careful modeling of the release ion density may be required for some aspects of the interaction. The release electron temperature is taken as 1 eV, consistent with expectations concerning the ionization process [e.g., Gurnett et al., 1986a]. Particles pass freely through both boundaries.

The ion populations are represented by $\sim 7 \times 10^4$ computational particles, which is sufficient to allow both the protons and lithium ions to be represented to minimum mass densities of < 1-2 proton masses per cubic centimeter. We therefore represent the parameter range over which mass loading dominates, rather than examining the effects of collective test ion motion (which has already been addressed, for instance, by Winske et al., [1985]).

Representing the ion populations by a finite number of computational particles n_c per cell of course also introduces a statistical fluctuation $\sqrt{n_c}$ in the ion bulk parameters, leading to noise in the electric and magnetic fields that are subsequently obtained from them at each time step. As the fields are not smoothed during the calculation (or in the results to be shown here throughout) in order to avoid loss of resolution, the signal to noise ratio in the fields is just $\approx \sqrt{n_c}$ also. We have

verified that this is the case by repeating the simulation run for a range of values of n_c (spanning approximately half an order of magnitude), and it is then found that provided that the statistical fluctuations are sufficiently small in magnitude (<40 % at worst in any cell in the entire simulation box), the results to be presented here are independent of n_c. The simulation run to be discussed in the next section has in general statistical fluctuations in n_c of ~ 15% in the computational particle population representing the protons and ~ 5% in that representing the release ions, chosen to be well inside this limit.

For the initial and boundary conditions on the fields we need only specify $\underline{B}$ along with the particle properties to specify $\underline{A}$, calculating the electric fields self-consistently within a time step. Here the ambient 10 nT field, lying wholly in the $\hat{z}$ direction, is reduced to zero on the spatial scale with which the release ion density is increased, effectively imposing "diamagnetic" currents to simulate the observed cavity. Additionally, this keeps the downstream ion behavior as simple as possible. It is important to note, however, that if a cavity is not imposed as an initial condition the field structure downstream of the region where the two ion populations interact would in general not be expected to be suppressed to zero. The diamagnetic currents required to do this cannot be generated spontaneously from the massless electron fluid, in which we have effectively shrunk the electron gyroradii to zero. It is probably in this respect that our hybrid representation is least like the overall observed behavior of the releases. In test runs, however, we have found that the ion interaction to be discussed here does not differ appreciably whether or not a magnetic cavity has been imposed downstream, although the ion motion in the downstream region is deflected slightly by the presence of the field.

In previous global hybrid simulations of the releases [e.g., Lui et al., 1986; Brecht and Thomas, 1987], field depressions were found to form which are located behind the obstacle, i.e., in the wake region, rather than at the release center where the field instead becomes enhanced. This is perhaps not surprising, since from the above discussion these field depressions would not be expected to represent the diamagnetic response of the actual release electron cloud, instead being a "wake" in the ambient massless electron fluid (and its, to some extent, "frozen-in" flux) that has encountered a still magnetized obstacle.

The constant resistivity acting on both ions and fluid electrons is taken to be $\eta^* = 2.6 \times 10^{-5}\ (\omega_{pi}\epsilon_0)^{-1}$ for the results to be discussed here. As a guide we have assumed that the layer carrying the diamagnetic current which "switches off" the field inside the magnetic cavity is sufficiently thick as to be stable against two-stream instability. The Penrose criterion gives an upper limit on the relative ion-electron drift speed u_0 for stability [Krall and Trivelpiece, 1973]:

$$u_0 < 1.3 \left[\frac{kT_e}{m_e}\right]^{\frac{1}{2}} \qquad \text{if} \quad T_e \gg T_i \qquad (7)$$

which via the approximation $neu_0 = J = \nabla \wedge \underline{B}/\mu_0$ translates to a lower limit on the scale thickness of the layer

$$L = \frac{\Delta B}{u_0 \mu_0 ne} > \frac{\Delta B}{1.3 \mu_0 ne} \left[\frac{m_e}{kT_e}\right]^{\frac{1}{2}} \qquad (8)$$

Given the typical observed field jump of $\Delta B \sim 40$ nT and our release density $n = 100\ cm^{-3}$, we have $L > 5$ km. Equating this scale with a resistive scale length $L_\eta = \eta/v_0\mu_0$ suggests, for bulk speeds $v_0 \sim 500\text{–}50$ km s^{-1}, resistivities of $\sim 7.5 \times 10^{-5} - 7.5 \times 10^{-6}\ (\omega_{pi}\epsilon_0)^{-1}$, from which we have chosen a typical value. It must be noted, however, that the ratio T_e/T_i in the diamagnetic layer is not well known, and that if $T_e >> T_i$ the Penrose criterion requires $u_0 < \sqrt{(kT_i/m_i)}$, giving larger values for the boundary thickness. The choice of L_η must also be influenced by the observations themselves, which suggest [e.g., Lühr et al., 1986a, b] boundary thicknesses of about a few kilometers depending of course on the speed at which the IRM is believed to exit the cavity. The numerical experiment discussed here has been repeated for values of η ranging above and below our chosen value by 2 orders of magnitude in total, over which it is found that the gross features to be discussed in the next section remain unchanged.

Although the results to be presented here are for lithium release ions, we have also conducted numerical experiments using release ions of different masses in order to investigate their applicability to a barium release. The requirements of a consistently low statistical noise level and the representation of a minimum mass density of release ions which is much less than the mass density of the oncoming proton flow imply that the number of computational particles used to represent the release ions must just increase linearly with the release ion mass (all other parameters kept constant). Therefore for the purpose of a comparative numerical experiment it is not feasible to compare lithium (mass 7 m_p) and barium (mass 137 m_p). However, simulations with the release ion mass ranging from 3 m_p to 28 m_p all reveal qualitative behavior identical to that which will now be presented in the next section.

3. Results

We will now present the results of a single run, with the initial conditions given in the previous section. The real time spanned by this run, ~ 1 s, was chosen to be sufficiently long to allow the interaction to evolve into an approximately steady configuration, rather than to represent a significant fraction of the lifetimes of the diamagnetic cavities of the releases as seen by the IRM (~ 6 s for lithium, ~ 80 s for barium).

3.1. Initial Transient Behavior

The situation soon after t = 0 (at t = 0.2 s) is shown in Figure 1. Here, the plasma parameters, fields, and samples of the individual particle velocities are all plotted versus the direction of variation, $\hat{x}$, across the computational "box" with all parameters expressed in SI units (or convenient multiples of them). The locations of regions of particular importance will be marked with vertical broken lines. The upstream boundary where the undisturbed solar wind enters is on the left-hand side of the plot, and the downstream boundary, where the lithium enters in a field free region, on the right-hand side. Moving from top to bottom, we can first see the proton and lithium number densities, in cm^{-3}, denoted by the thick and thin lines, respectively, which have not changed appreciably from their values at t = 0. The $\hat{z}$ component of the magnetic field (in nanoteslas) can be seen to have compressed in front of the region where the release ion density becomes substantial, to a maximum (at vertical broken line A) of ~ 32 nT, the flux contained in this field compression just corresponding to that associated with the solar wind protons which have arrived in the

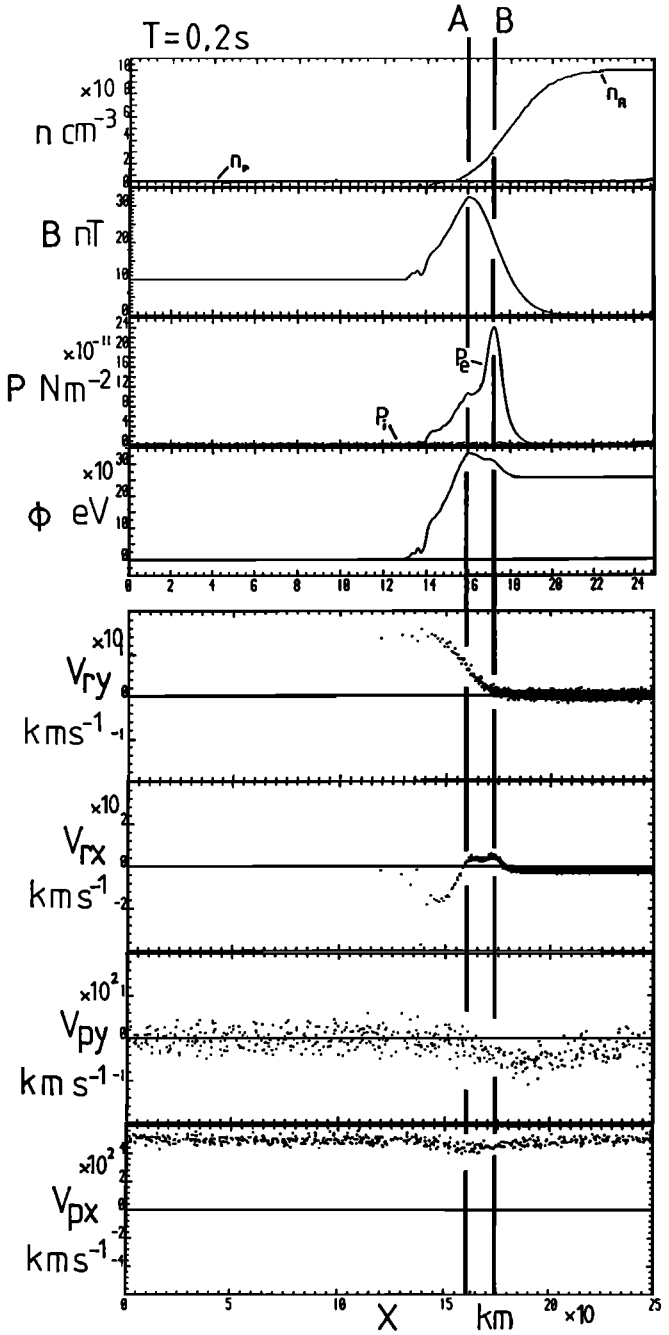

Fig. 1. Plasma parameters, fields, and $V_{x,y}$ phase space configuration shortly after the beginning of the simulation run discussed in the text, at t = 0.2 s. All parameters are plotted versus x, the direction of variation of our simulation, and are expressed in SI units or convenient multiples of them. This same format will be used to show the time development of these parameters in subsequent figures. The upper four panels show bulk parameters (the ion densities, magnetic field strength, ion and electron thermal pressures and potential), and the lower four panels show x and y velocity phase space plots of the release ions and protons respectively. The vertical broken lines labeled A and B at the top of the figure denote the locations of distinct features in the subsequent development of the ion interaction (i.e., the peak in the magnetic field and, downstream of it, in the electron pressure, along with corresponding features in the ion behavior), the significance of which is discussed in the text.

previous 0.2 s and have passed freely through the release plasma. The $\hat{y}$ component of $\underline{B}$ is set to zero as an initial condition and due to the planar geometry enforced by the one-dimensionality of the model remains so throughout the simulation. The next panel shows the total thermal ion pressure and electron pressure in Newtons per square meter. The local enhancement of the electron pressure, by a factor of ~ 300 from its initial solar wind value of ~ 9.4×10^{-13} N m^{-2}, is principally due to electron heating through the resistive terms in the electron fluid equations. These depend upon the current, so that the electron pressure peaks at the maximum magnetic field gradient (position B), downstream of the magnetic field peak. By comparison, the ion pressure at this time is negligible within the field pileup region, having changed little from its value at t = 0.

The next panel shows the potential (in volts) arising from the $\hat{x}$ component of the electric field (i.e., $E_x = -\partial\varphi/\partial x$). The behavior of E_x, and hence φ, can be seen from (6) to depend upon the electron pressure gradient and the magnetic field gradient (since $V_e \approx -J/ne$).

Moving from left to right across the plot we see that the potential first rises, corresponding to an upstream pointing x electric field which slows down the oncoming protons and accelerates upstream release ions in the $-\hat{x}$ direction. The potential reaches a maximum at A, i.e., at the peak in the magnetic field, and falls away to provide a downstream pointing x electric field which acts to accelerate downstream both release ions and protons. The bottom four panels of Figure 1 are of the v_x and v_y phase space of both the oncoming protons and release ions. The effect of the potential can be seen clearly in the particle v_x phase space plots. The proton v_x decreases in the region where φ first increases. The corresponding region in the lithium x velocity plot shows ions being accelerated upstream ($v_x < 0$) by this same potential. The lithium x velocity changes sign at A just at the point where the potential maximizes, ions to the right of this region being accelerated downstream. The double-humped structure in the downstream-moving ($v_x > 0$) lithium beam can be seen to correspond to that in the potential (i.e., to the peaks in P_e and B).

The asymmetric potential structure (note that the potential at x > B does not return to its upstream value) or, equivalently, the resulting asymmetric bipolar E_x electric field enables an exchange of $\hat{x}$ momentum from solar wind protons traversing this region to the release ions. We can also see from the phase space plots that upstream of the electron pressure peak (x < B), in the region where the magnetic field is enhanced, an exchange of momentum in the $\hat{y}$ direction occurs between the protons and release ions. At sufficiently early times, the $\hat{y}$ direction in our simulation would correspond approximately to the $-\underline{U}_\alpha \wedge \underline{B}$ convection electric field direction (where $\underline{U}_\alpha$ is the relative velocity ($\underline{V}_e - \underline{V}_\alpha$) between an ion species bulk flow $\underline{V}_\alpha$ and the bulk velocity of the single massless electron fluid). We would then expect release ions in the region outside the field cavity to begin to move in the $+\hat{y}$ direction as they are "picked up" by the local convection electric field in which they are created approximately at rest. If, instead, we transform into the rest frame of the solar wind, in the region upstream of the magnetic cavity where the release ion density is still significant, the protons would now be at rest and, by virtue of the oncoming electron flow, would be picked up by a local convection electric field pointing in the $-\hat{y}$ direction of our simulation. As the two species exchange momentum, the electron flow direction will of course deviate from its initial value implied in the above description.

We can see the effect of this "$\underline{U}_\alpha \wedge \underline{B}$" directed momentum transfer along with the longitudinally ($\hat{x}$)

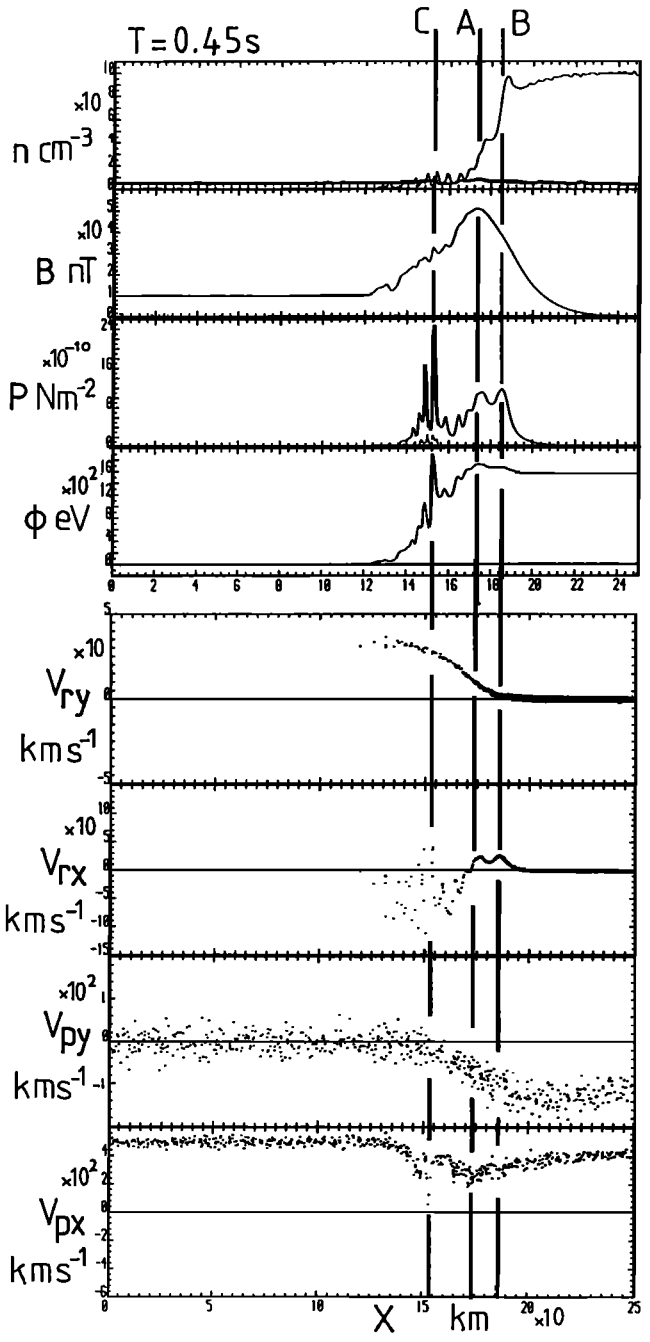

Fig. 2. Situation for the run discussed in the text at a later time, t = 0.45 s. The same parameters are plotted in the same format as in Figure 1,, but on different vertical scales, for clarity. The broken lines labeled A and B refer, as in Figure 1, to the peak in the magnetic field and in the electron pressure downstream of it; the location of a new feature in the electron pressure that has formed upstream is marked with broken line C. The corresponding behavior of the ions, which may be seen in the velocity space plots, and its significance for the interaction as a whole are discussed in the text.

directed momentum exchange (also illustrated in Figure 1) from a multifluid description for the plasma as given, for instance, by Chapman and Dunlop, [1986]. The x, y, and z components of this momentum equation for the αth ion species appropriate to our simulation become (i.e., with $J_x = 0$, $\underline{B} = B_z\hat{z}$, no photoionization)

$$m_\alpha n_\alpha \frac{DV_{x\alpha}}{Dt} = en_\alpha\left[V_{y\alpha} - \frac{1}{n}\sum_{\alpha'} n_{\alpha'}V_{y\alpha'}\right]B_z \qquad (9a)$$

$$- \frac{n_\alpha}{n}\frac{d}{dx}\left[\frac{B_z^2}{2\mu_0} + P_e\right] - \frac{dP_{x\alpha}}{dx}$$

$$m_\alpha n_\alpha \frac{DV_{y\alpha}}{Dt} = -en_\alpha\left[V_{x\alpha} - \frac{1}{n}\sum_{\alpha'} n_{\alpha'}V_{x\alpha'}\right]B_z \qquad (9b)$$

$$m_\alpha n_\alpha \frac{DV_{z\alpha}}{Dt} = 0 \quad \text{with} \quad \frac{D}{Dt} \equiv \frac{\delta}{\delta t} + \underline{V}_\alpha.\nabla \qquad (9c)$$

where the electrons have been treated as a single massless, charge-neutralising fluid. From the y equation it is immediately clear that, in the geometry employed here, momentum exchange in this direction between the ions always arises only as a component of the $\underline{U}_\alpha\wedge\underline{B}$ directed momentum transfer discussed above. In the case of very early times, when in the simulation frame $\underline{V}_R \approx 0$, $\underline{V}_p \approx V_{px}\hat{x}$, the $\hat{y}$ equation for the protons and release ions respectively reduces to

$$m_p \frac{DV_{py}}{Dt} = -e\frac{n_R}{n}V_{px}B_z, \qquad m_R \frac{DV_{ry}}{Dt} = e\frac{n_p}{n}V_{px}B_z \qquad (10)$$

with the equivalent $\underline{U}_\alpha\wedge\underline{B}$ term on the right-hand side of the $\hat{x}$ equation vanishing. This is just as expected from the above discussion, both species being significantly deflected where $n_p \approx n_R$. When one species dominates the other substantially, we approach the "test ion" limit, the more dense of the species being essentially unperturbed and defining to a good approximation the ambient flow $\underline{U}_\alpha$ and convection electric field $\underline{E}_c = -\underline{U}_\alpha\wedge\underline{B}$ in which the less dense species accelerates. Ion motion in the $\hat{x}$ direction, on the other hand, is determined by the magnetic field and pressure gradients, as well as the remaining component of the $\underline{U}_\alpha\wedge\underline{B}$ directed force.

3.2. Field Saturation/"Snowplough" Formation

The behaviour found at early times continues until t ~ 0.45 s, with the magnetic field increasing in magnitude due to the addition of flux that has been brought by oncoming protons which still freely pass through the release plasma. Around this time, however, the magnetic field maximum saturates at a value of ~ 50 nT. The corresponding changes in the remaining parameters can be seen in Figure 2, which shows the situation at t = 0.45 s, all parameters being plotted in the same format as in the previous figure, but with different vertical scales. From the top panel we can now see that whereas the proton density has remained relatively uniform up to this time, the release ion density has formed a "spike" at x ~ 188 km and to a lesser extent at x ~ 176 km. Both these structures in the density lie downstream (i.e., in +x) of the peaks in the magnetic field and electron pressure (at A and B, respectively) and can be seen to correspond to features in the potential. These density enhancements in the release ion population correspond to the double-humped population of release ions that are accelerating downstream (cf. the v_x phase space plot). From the y phase space plots we can also see that the y velocity (i.e., due to "$\underline{U}_\alpha\wedge\underline{B}$" acceleration) of the more dense spike downstream of B is small compared with its x velocity. Well upstream of this region, at

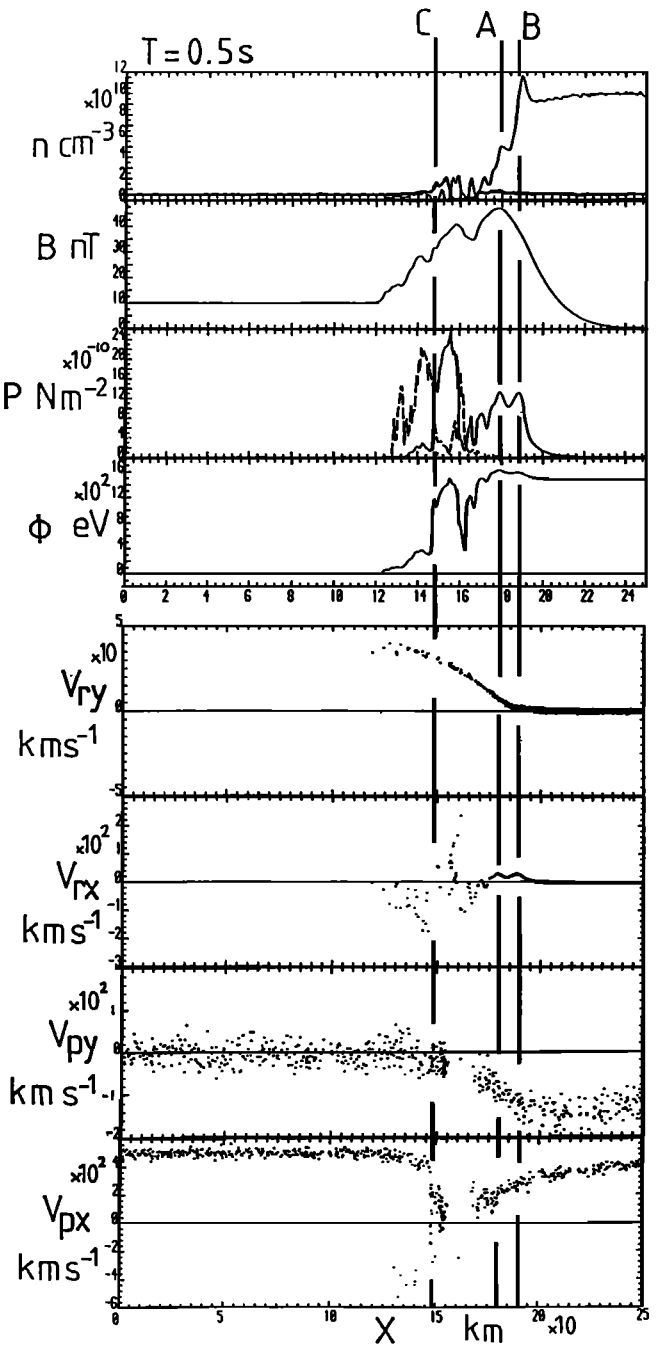

Fig. 3. Further time development of the simulation run discussed in the text, at t = 0.5 s. The format is the same as in the previous figures, parameters once again being plotted on different scales. Note that only one in every 30 computational particles are plotted in the phase space plots, so that the absence of points in some regions implies that the density is small, but not necessarily zero, there.

x ~ 140–160 km (i.e., at C), the electron pressure has increased dramatically. The fine structures in P_e and hence E_x will of course depend strongly on the choice of η and Δx, but their overall morphology and magnitude are found to persist through changes in the resistivity and grid size of several orders of magnitude (until these become so large that the structure cannot be resolved). The net result is to produce a potential which is sufficient to substantially retard the oncoming protons (which have a mean energy of ~ 1300 eV), as can clearly be seen in the proton v_x phase space plot. The release ions in this upstream region are strongly scattered in their x velocity by fluctuations in the x electric field (corresponding to fluctuations in the electron pressure gradient) but on the whole move upstream. Their transverse motion in ~ $-\underline{U}_{o\wedge}\underline{B}$ $(+\hat{y})$ is once again balanced by a deflection of the protons in the opposite (i.e., $-\hat{y}$) direction. Notice that the protons within the release region have acquired $\hat{y}$ velocities comparable to their $\hat{x}$ velocity.

The situation a short time later is shown in Figure 3, at t = 0.5 s. Here we can see that the release ion density profile has steepened, the downstream spikes (just downstream of x = A and B) having increased in magnitude and moved further downstream, along with their corresponding accelerating potential structure. The potential profile in the upstream region at and just downstream of C can be seen to closely follow the variation in the electron pressure, rather than the magnetic field. It is this upstream potential jump which (as can be seen from the proton x velocity phase space plot) begins now to sharply decelerate and even reflect the oncoming protons. The proton number density is hence first enhanced just downstream of C and then depleted downstream of the maximum in the potential. The corresponding regions in the phase space plots show gaps in the ion populations, where the density is small.

The total ion pressure just upstream of this potential jump (at C) is strongly enhanced by the presence of the backscattered protons, reaching values which are just equal to the magnitude of the electron pressure just downstream. Since the electron pressure dominates over the magnetic pressure at this location (as will be shown to be the case), this boundary is roughly in pressure balance and hence approximately static in the frame of reference of the simulation. On the downstream side of this electron pressure and potential peak, i.e., at x ~ 160 km, there is a "well" in the potential. From the release ion x velocity phase space plot we find that a population of ions interacts with this potential structure and is scattered to large x velocities. This population forms the principal component of the peak in the ion pressure at x ~ 160 km. The potential structure thus begins to divide the release ions into three populations at this time: those accelerated upstream along with the reflecting protons which are located upstream of C, those interacting with the potential well and the bulk of the release ions which are moved downstream en masse by the downstream propagating potential jump (principally at, and downstream of B). The transfer of momentum in the transverse direction (i.e., in y), as can be seen from the phase space plots, still proceeds as in the previous figures; that is, it is $\underline{U}_{o\wedge}\underline{B}$ directed.

3.3. Development of Quasi-Steady Structure

We can see how the interaction progresses in Figure 4, which shows the parameters at t = 0.55 s. At this time the principal release ion density spike has again moved further downstream (to x ~ 192 km, at B) and increased in magnitude as more release ions are "gathered up" by the downstream potential jump. This process by which most of the release ions are accelerated en masse by the downstream propagating potential jump is reminiscent of the "snowplough" process [e.g., Krall and Trivelpiece, 1973], although in the latter only the magnetic field pressure is considered to constitute the driving force. The well in the potential has at this stage nearly disappeared, leaving a potential jump at x ~ 160

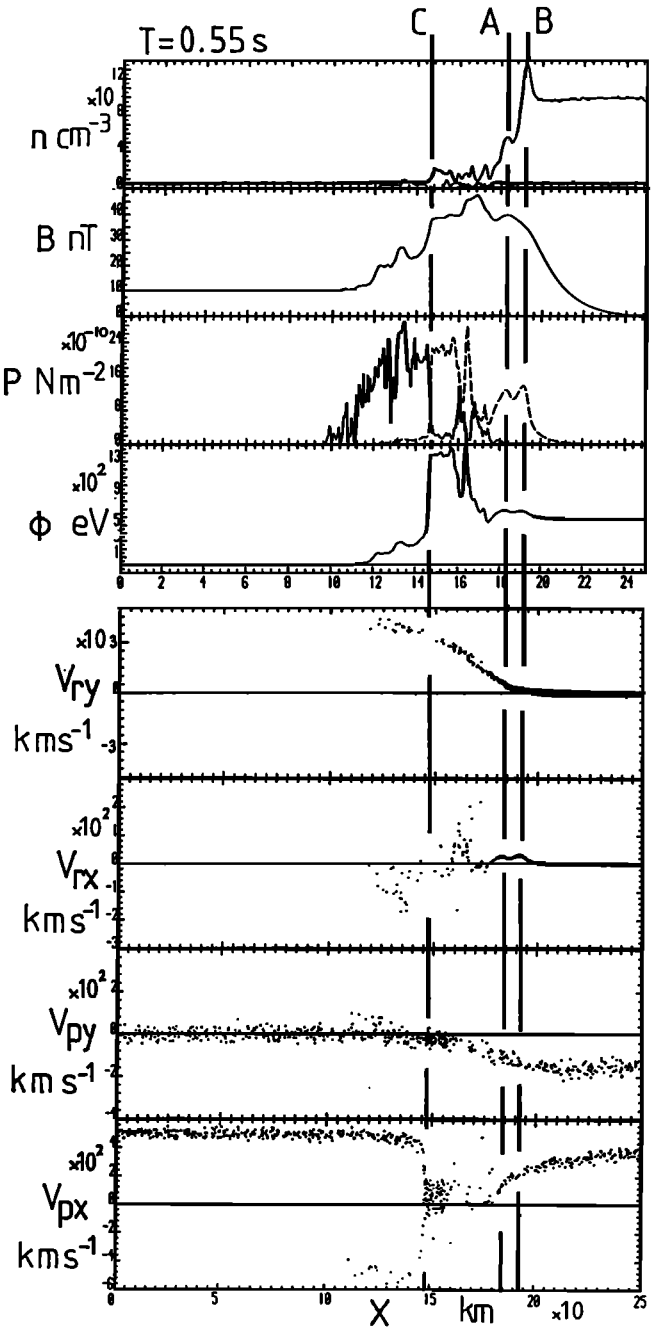

Fig. 4. Situation for the simulation discussed in the text at a later time t = 0.55 s, once again in the same format as in the previous figures.

km which will now systematically accelerate the release ions in this region downstream. Hence in the x velocity phase space plots we see that the central release ion population (downstream of C) is now moving downstream at large velocities, so that it will eventually overtake the snowploughed density spike. In a release cloud of finite extent this population would form a "tail" pointing downstream of the bulk of the release ions, but retaining some transverse ($\hat{y}$) velocity at this stage.

The magnetic field profile at this time begins to acquire some detailed structure. Features in the piled-up magnetic field closely correspond to the locations of enhancements in the ion densities (and ultimately to features in the potential). We can see that the four turning points in $|\underline{B}|$, at x ~ 130 km, at ~ 148 km, (i.e., at C), at ~ 168 km, and ~ 184 km (i.e., at A), correspond in turn to the upstream moving release ions (moving with the reflected protons), the slowed protons which accumulate just downstream of the first potential jump where they have been decelerated, the release ion tail population (at the downstream edge of the potential maximum or "overshoot"), and a region where the release ion density is enhanced, just upstream of the snowplough density spike itself. The ion behavior leading to this structure in the density is perhaps clearest in the phase space plots. The overshoot in the potential begins to separate the upstream and downstream moving components of the release ion density, depleting the release ion density at C (see also top panel), where the proton density peaks. Similar symmetric behavior is associated with the downstream side of the potential overshoot at x ~ 168 km, where the proton density is depleted and the release ions are swept up to form the tail population. To some extent, fine details in the magnetic field profile suggested by our model are influenced by the choice of initial release ion density profile, as this in turn will affect, for instance, the proportion of release ions which at later times are found upstream of the accelerating potential as opposed to downstream.

Our final figure from this time sequence, Figure 5, shows the situation at t = 0.75 s. At this time the snowploughed density spike has moved further downstream, to a region where the initial release density profile is approximately constant. This density spike now moves at a constant downstream velocity, in this case of 43 km s^{-1} ± 10%. We shall see later that this is a direct result of the constant release density profile in this region. The total ion and electron pressures still balance at the upstream potential jump (that is, at C). Equivalently, since the electron pressure dominates the magnetic field pressure at that location, this is just consistent with the upstream potential jump remaining approximately static. The locations where the protons (x ~ C), the tail release ion population (x ~ A) and the snowploughed release ions (x ~ B) are accelerated by the potential have become well separated by this time as the latter two have moved downstream. This can be clearly seen in the potential, magnetic field, and pressure profiles. The quasi-steady potential morphology which has now formed maintains a high potential plateau in the region between C and A. This structure tends to separate the upstream ion population from the tail and snowplough populations and prevents migration between the upstream and downstream regions. Careful examination of the individual release ion locations at this time, and at subsequent times shows this to be the case. The potential jump that accelerates the release ion tail population at A is now clearly coincident with the magnetic field peak and has decreased in magnitude. As a consequence, the x velocity phase space plot reveals that ions swept up by this potential are not accelerated to as large a speed as those which interacted earlier in time, and which have now begun to overtake the snowplough population. The entire tail population can at this time also be seen to be moving at relatively small transverse velocities.

The behavior of the protons that have been slowed by the potential jump at C, and that are located just downstream, now becomes clear. This population just moves downstream with the same constant bulk speed as the release ion snowplough population. The proton population that has been reflected from the potential jump can now be seen moving upstream and acquiring motion in the + $\hat{y}$ direction as the protons begin to

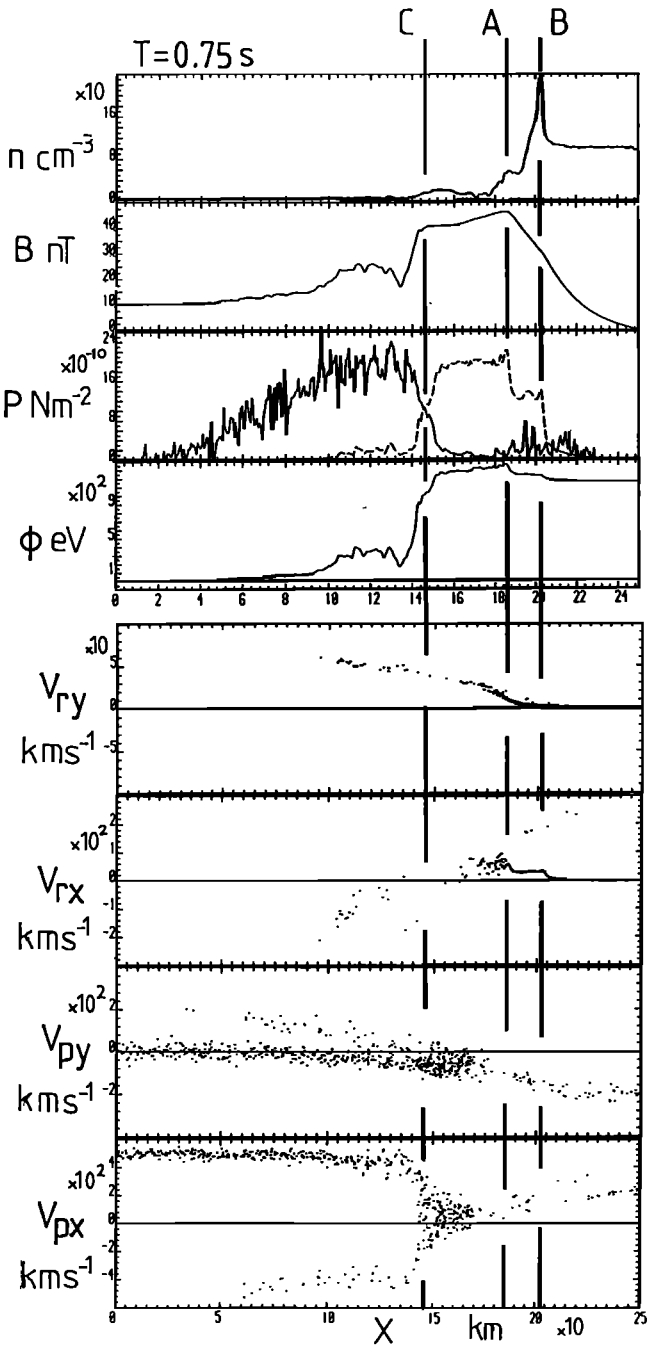

Fig. 5. Final figure in the time sequence for the simulation run discussed in the text and is once again in the same format as the previous figures. At this time, t = 0.75 s, the field and plasma have reached a quasi-steady configuration which effects momentum transfer between the oncoming protons and release ions.

gyrate in the upstream B field. Ultimately in the planar geometry used here these protons would complete their gyromotion and return to interact with the release plasma. However, since the dimensions of the release cloud are known to be much smaller than the characteristic gyroradii of these gyrating protons, it is not appropriate to consider the effect of their behavior over an extended part of their gyromotion. Instead we have removed from the simulation backstreaming protons which have a y displacement of the order of the dimensions of the actual AMPTE lithium releases, on the premise that these particles would not contribute to the upstream conditions that affect the momentum transfer process. Since the UKS-IRM separation of ~ 30 km for the lithium releases represents an upper limit on this scale size, the value of 8 km used here is not unreasonable. The number of computational particles removed from the simulation in this way represents < 8% of the solar wind population that flows into the left-hand side of the box during the ~ 0.75 s of the run shown here. For sufficiently small values of the computational box length (i.e., in the $\hat{x}$ direction) it is of course possible for the backstreaming proton population to eventually exit the left-hand (or upstream) boundary of the box before moving a distance in the $\hat{y}$ direction which is comparable to the scale size of the release obstacle. This would effectively disrupt the left-hand boundary conditions, so that the simulation results would no longer be physically meaningful. The physics of the simulation also breaks down when the downstream propagating field structure finally reaches the right-hand boundary of the box, and it is just this situation which brings the simulation discussed here to an end.

3.4. Summary of Simulation Results

We will summarize the entire sequence of events by examining the net forces that act on the plasma as a whole. An expression for this in terms of the individual ion species can be obtained from (9), the general form of which is

$$\rho_\alpha \frac{\partial \underline{V}_\alpha}{\partial t} + \rho_\alpha \underline{V}_\alpha . \nabla \underline{V}_\alpha = e n_\alpha \left(\underline{V}_\alpha - \frac{1}{n} \sum_{\alpha'} n_{\alpha'} \underline{V}_{\alpha'} \right) \wedge \underline{B} - \frac{n_\alpha}{n} \nabla . (\underline{\underline{T}} + \underline{\underline{P}}_e) - \nabla . \underline{\underline{P}}_\alpha \qquad (11)$$

where the "$\underline{j} \wedge \underline{B}$" force has been expressed for convenience in terms of the Maxwell stress tensor $\underline{\underline{T}}$. Adding $\underline{V}_\alpha$ times the continuity (of mass density) equation to both sides of (11) and summing over all α gives

$$\sum_\alpha \frac{\partial}{\partial t} (\rho_\alpha \underline{V}_\alpha) = \sum_\alpha \nabla . (\rho_\alpha \underline{V}_\alpha \underline{V}_\alpha + \underline{\underline{P}}_\alpha) + \nabla . (\underline{\underline{T}} + \underline{\underline{P}}_e) \qquad (12)$$

the $\underline{U}_\alpha \wedge \underline{B}$ term which describes momentum transfer between the species locally having now vanished over this summation. Therefore in the context of our one-dimensional simulation, only the x components of the terms on the right-hand side of (12) will be nonzero. Here, in Figure 6, for each of the times already discussed (except t = 0.55 s) we shall compare the total "pressure", given by integration of the right-hand side of (12):

$$P_T(x) = \sum_\alpha \rho_\alpha V_{\alpha x}^2 + \sum_\alpha \frac{\rho_\alpha k T_{\alpha x}}{m_\alpha} + \frac{B_z^2}{2\mu_0} + P_e \qquad (13)$$

with the individual magnetic and electron partial pressures $B_z^2/2\mu_0$ and P_e. Regions where this total pressure changes will hence be just those where the rate of change of the total plasma momentum is nonzero. The significance of the magnetic and electron partial pressures can be seen from (6), since assuming $J_y \simeq -ne V_{ey}$ this integrates to give

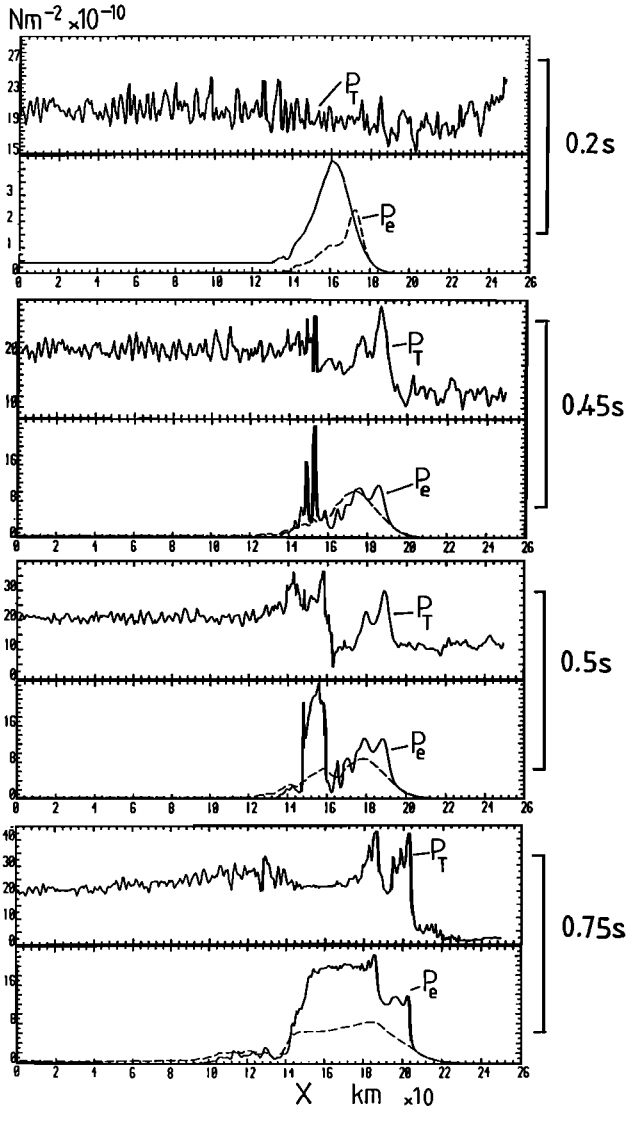

Fig. 6. A comparison between the total pressure P_T (defined in the text) and the contributions of the electron (P_e) and magnetic ($B^2/2\mu_0$) pressures. In order to distinguish between the three curves, the total and electron pressures have been labeled. This comparison has been made for each of the times for which simulation parameters have been plotted in the previous figures (except for T = 0.55 s); the time is marked on the right of each corresponding pair of panels. All parameters are in convenient multiples of SI units, although the vertical scales vary for clarity.

$$\int_0^x ned\varphi = \frac{B_z^2(x) - B_z^2(0)}{2\mu_0} + P_e(x) - P_e(0) \qquad (14)$$

As the ion current is found in general to be less than ~ 5% of the total current, (14) implies that changes in the magnetic and electron pressures alone simply contribute to the potential which, as we have already seen, plays a major role in the dynamics of the various ion populations. The behavior at early times (t = 0.2 s) is shown at the top of Figure 6. From the scales on the ordinates of the first two plots we can see that the total pressure exceeds either the magnetic or electron pressure and is essentially just that of the ram pressure of the incoming solar wind protons which freely pass through the release cloud. The total pressure is therefore approximately constant, indicating no large-scale bulk acceleration of the plasma at this stage. The slight decrease in P_T just downstream of the peaks in the electron and magnetic pressure is just consistent with the release ion acceleration that is beginning to take place at this time. We have seen that this is the result of the electron and magnetic pressures producing an asymmetric bipolar x electric field (i.e., a maximum in the potential as in Figure 1). The upstream side of this electric field (at x ~ 150 km) is dominated by the magnetic field gradient, while the downstream side (at x ~ 170 km) includes contributions from both partial pressures. The sum of these partial pressures just produces a double hump in the potential, the effect of which can be seen directly in the release ion x velocity phase space plot of Figure 1. Thus momentum exchange in the x direction at this stage is achieved directly via both electron pressure gradients and the pressure of the piled up magnetic flux. Resistive electron heating in the regions of magnetic field gradient is already occurring, however, producing the peak in P_e at x ~ 172 km. Hence this downstream peak in P_e is always on the downstream side of the magnetic field peak, where it subsequently always forms the downstream potential jump acting on the snowploughed release ions.

This heating continues until the electron pressure begins to become comparable to the oncoming solar wind ram pressure. This occurs at t ~ 0.45 s and is shown in the next two panels of Figure 6. At this stage the electron pressure profile has evolved two peaks corresponding to the upstream and downstream gradient maxima in the magnetic field. The magnetic field has reached its maximum peak value at which it remains (approximately) throughout the remainder of the run. The upstream peak in P_e (at x ~ 150 km) is noisy but has grown significantly larger than the magnetic pressure peak; it is responsible for a potential which substantially retards the oncoming protons, as can be seen in Figure 2, so that at this location the total pressure decreases sharply. The downstream peak in P_e (at x ~ 180 km) is just downstream of the magnetic pressure peak, and since in this region P_e is approximately twice as large as $B^2/2\mu_0$, the exchange of x momentum between the protons and the release ions can still be seen from the phase space plots of Figure 2 to be proceeding in a manner similar to that at earlier times, namely, via the potential with comparable contributions from both magnetic and electron pressure gradients. The drop in total pressure after x ~ 200 km corresponds to a decrease in the ram pressure of protons which at this stage have been decelerated by the structure associated with the downstream peak in P_e and which have passed through the simulation box before the upstream peak in P_e had formed. Finally, the accelerated release ions can be seen to correspond to the peaks in the total pressure at x ~ 186 km and x ~ 174 km.

By the slightly later time (t = 0.5 s) shown in the third pair of panels, the electron pressure has further evolved so that the upstream peak dominates the magnetic pressure. This then provides the potential jump which retards the oncoming solar wind population and reflects a fraction of it. The counterstreaming protons that this produces upstream provide a sufficiently velocity-dispersed population to be in pressure balance with the electron fluid (see Figure 3). This continues to be the case throughout the simulation run and is consistent with the fact that this upstream jump in the electron pressure (and

hence the potential) remains approximately static in our simulation frame. The total pressure therefore remains approximately constant as we move through this region downstream (in +x) until x ~ 160 km, where the proton density drops and the ions are scattered by a well in the potential, due as we see here to the minimum in the electron pressure. Downstream of this location the electron and magnetic field pressures are still of the same order, providing the snowplough potential as at earlier times.

The ratio of electron to magnetic pressure does not change appreciably at later times, as can be seen from the bottom two panels, showing the situation at t = 0.75 s. Here, however, the electron pressure minimum has disappeared and with it the well in the potential. Consequently the total pressure is now approximately constant throughout the region of piled up flux and enhanced electron pressure, dropping just as we move downstream of the snowploughed release ion population. The two peaks in the total pressure, at x ~ 180 km, and ~ 200 km, once again correspond to the release ion tail and snowplough populations. In this final steady configuration we can identify several well-defined and separated features. The upstream region contains counterstreaming protons and release ions. Solar wind protons are retarded and/or reflected at the location of a sharp rise in both magnetic and electron pressures. The magnetic field then continues to rise further downstream to its peak, which coincides with the tail release ion population. Finally, the smowploughed population is located downstream of the magnetic field maximum, since it is here that the downstream electron pressure peaks, producing the corresponding driving potential. The two sharp gradients in the total pressure just correspond to the regions where the release ion tail and snowplough populations are located, indicating that it is only within these restricted regions that a net rate of change of the total plasma momentum occurs. This implies that we can construct a simple analytical model which, to a first approximation, will describe the steady motion of the snowploughed release ion population, and this is done in the next section. In principle, such a model would yield an estimate of the snowplough speed as a function of the given parameters of any particular release and oncoming flow.

Finally, it is perhaps worth comparing the results presented here with those of a previous one-dimensional hybrid simulation performed by Lui et al., [1986]. Although the principles of their calculation are similar to those used here, their methodology differs principally in two respects. First, in order to resolve the details of the interaction region, we have in our simulation employed a larger number of simulation particles over a grid which represents finer resolution in real space. Secondly, the initial profile of the release ion density, a Gaussian ~ 30 km in extent, chosen by Lui et al. to examine the behaviour of the entire release cloud, leads to a sharper release ion density gradient than that used here. Thus the region over which the release population is initially introduced occupies a smaller fraction of their simulation box, further reducing the effective resolution of the interaction region, which takes place on a scale dominated, at least initially, by the scale upon which the initial release density profile varies. Hence the gross features found by Lui et al., namely, release ions being accelerated downstream and protons being slowed and reflected in a region of enhanced magnetic field, are consistent with those reported here. In this analysis, however, key features of the momentum transfer process have been revealed as a consequence of improved resolution of the boundary layer structure.

3.5. Estimate of the Snowplough Speed

First, we assume that a stream of protons (with initial speed V_{sw} at constant number density n_{sw}) interact with the snowplough field structure, suffering an effective collision with coefficient of restitution ϵ. Neglecting any transverse motion, in the frame moving with the snowplough, at speed V_{sp} their velocity after the interaction is just $-\epsilon(V_{sw}-V_{sp})$. Their change in momentum in the rest frame (in which the proton speed is V_{sw}) is then $\Delta P_x = -(V_{sw}-V_{sp})(1+\epsilon)m_p$, so that, since the particle flux interacting with the snowplough is $n_{sw}(V_{sw}-V_{sp})$ the rate at which momentum is delivered to the snowplough is

$$\frac{dP_{sp}}{dt} = -\frac{dP_{sw}}{dt} = (1+\epsilon)\, m_p n_{sw}(V_{sw}-V_{sp})^2 \qquad (15)$$

The moving snowplough field structure encounters the release ions which are approximately stationary in our rest frame. The simulation results suggest that on interacting with the snowplough these ions are simply accelerated to the snowplough speed V_{sp}, so that (with subscript R denoting the release ion population) at any time t the momentum tranferred to newly snowploughed ions is

$$\frac{dP_{sp}}{dt} = n_R(x_{sp}(t),t)\, m_R V_{sp}^2 \qquad (16)$$

where $x_{sp}(t)$ is the position of the snowplough at time t. Equation (16) implicitly assumes that ions only interact once with the snowplough, which will be true provided that V_{sp} is constant or decreasing (i.e., $dV_{sp}/dt \leq 0$). In this case we can equate (15) and (16) to give

$$V_{sp} = \frac{\alpha}{1+\alpha} V_{sw} \approx \alpha V_{sw} \qquad \alpha = \left[\frac{(\epsilon+1)\, n_{sw} m_p}{n_R(x_{sp}(t),t) m_R}\right]^{\frac{1}{2}} \qquad (17)$$

The condition $dV_{sp}/dt \leq 0$ then becomes $Dn_R/Dt = (\partial/\partial t + V_{sp}.\partial/\partial x)n_R \geq 0$, that is, when the snowplough moves into regions of ever increasing or constant release number density. This is just the situation that arises with the simplified release ion number density profile used in our simulation, so that we can immediately compare the estimate given by (17) with the value for the 'snowplough' speed given by the simulation results. First, the proton behavior seen in the quasi-steady configuration (i.e., Figure 5) is that the majority, after interacting with the upstream retarding potential jump at C, move downstream with a bulk speed which is just the snowplough speed of the release ions, to a good approximation. Hence it is appropriate to choose $\epsilon = 0$, and with the release ion density of ~ 100 cm^{-3} in (17) we find $V_{sp} \simeq 42$ km s^{-1}, which is in excellent agreement with the results of the simulation.

In regions where $Dn_R/Dt < 0$ the snowplough speed increases so that it "catches up" with release ions accelerated at earlier times and interacts with them more than once. The assumption implicit in (16) and (17) are hence no longer appropriate; we can instead assume that momentum is transferred from the oncoming protons to the entire mass of release ions M which have encountered the snowplough and are continually accelerated by it, so that

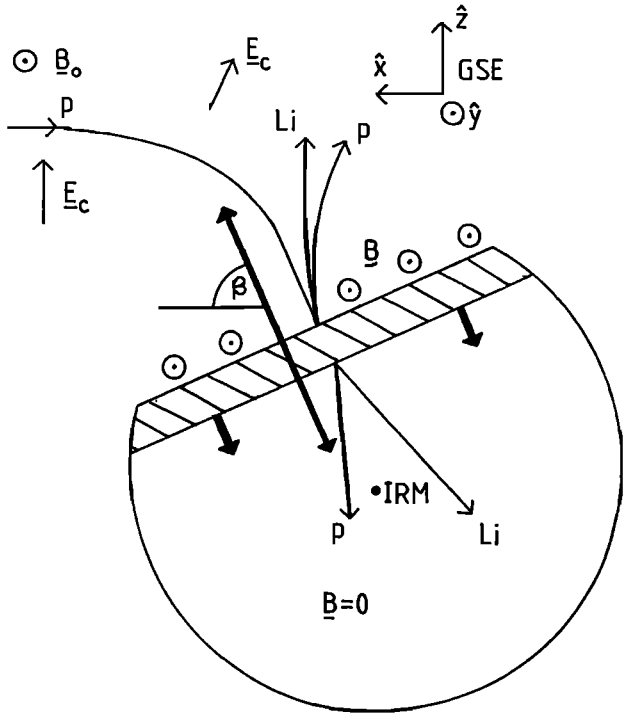

Fig. 7. A schematic diagram of the quasi-steady one-dimensional momentum transfer process revealed by the simulation discussed in the text, which has been set in the context of the three-dimensional release ion cloud. The plane of this simplified diagram is perpendicular to the ambient magnetic field $\underline{B}_0$ and contains both the oncoming proton flow direction $\underline{V}$ and convection electric field $\underline{E}_c = -\underline{U}_{R\wedge}\underline{B}$ (here for simplicity $\underline{V}$ is always perpendicular to $\underline{B}$; i.e., $\underline{B}$ always points out of the plane). Hence the release center also lies in this plane, and with it, the IRM spacecraft. The region spanned by our one-dimensional simulation is indicated by the thick, double-headed arrow, which will point at some angle β to the ambient flow direction (i.e., the $-\hat{x}$ GSE direction), as mass loading of the oncoming flow by release ions in this upstream region will deflect the proton flow direction as shown. These protons will then arrive at the decelerating potential jump (dashed line) and strongly compressed magnetic field region where a fraction become reflected. Release ions in this upstream region also move further upstream under the influence of this potential. Further downstream (i.e., on the edge of the diamagnetic cavity associated with the bulk of the release ions), the release ions become picked up en masse by a snowplough type process; this population, denoted by the hatched region, moves toward the IRM. The snowplough field structures also accelerate a fast release ion tail population which overtakes the snowplough population and moves through the cavity, along with the protons that have passed through the disturbed field structures.

$$\frac{dP_{sp}}{dt} = \frac{d}{dt}(MV_{sp}) = V_{sp}\frac{dM}{dt} + M\frac{dV_{sp}}{dt} \qquad (18)$$

with $$M = \int_0^t m_R\, n_R\, V_{sp}\, dt$$

which is identical to (16) except for the addition of the last term on the right-hand side.

Given an initial release density profile $n_R(\underline{r},t)$ along with the flow parameters upstream of the boundary it is therefore possible in principle to predict its approximate subsequent behavior produced by the formation of the snowplough field structure, using (15) and (18). Since, however, appropriate density functions for the actual releases (i.e., those that would be produced by an expanding cloud of photoionizing neutrals of finite extent) will in general be such that $Dn_R(x_{sp}(t),t)/Dt < 0$, requiring the integration of (18), we leave this detailed calculation to a further publication.

4. Implications for the AMPTE Releases

So far we have used the simplest possible geometry and a simple release ion density profile in order to investigate the general properties of the interaction that takes place between the release ions and oncoming solar wind proton flow. A steady field configuration is found to evolve which allows momentum to be transferred from the protons to the release ions on scales much smaller than their respective gyroscales as required for the initial stages of the AMPTE releases. Here we shall make a brief comparison between the results of the simulation and the release measurements, which first requires that the one-dimensional geometry used here is seen in the context of the three-dimensional release configuration.

An attempt to do this is shown in Figure 7, which is drawn in the plane perpendicular to the undisturbed magnetic field, containing the ambient solar wind flow direction and passing through the center of the release. For an idealized spherical release cloud the IRM also lies in this plane, and since we will for simplicity assume that the ambient $\underline{V}_{sw}\cdot\underline{B} = 0$, the magnetic field must everywhere be perpendicular to the plane (since on average $\underline{B}$ can only change direction by draping around the obstacle formed by the release, an effect not treated in our one-dimensional code since here $(\underline{B}.\nabla)\underline{B} = 0$). The plane hence also always contains the direction of the net local convection electric field $\underline{E}_c = -\underline{U}_{\alpha\wedge}\underline{B}$, shown on the figure for the release ions. On this sketch the results found from our one dimensional study will apply within a region around the release ion-population where the magnetic, electron, and ion pressure terms have become important in the momentum equations describing the motions of all the species involved (cf. (9) and (11)). Further from the release, where mass loading of the oncoming flow by release ions has become less dramatic, the first term on the right-hand side of (9) and (11) may dominate, so that the release ions will move more as "test" particles, accelerated by principally the local $-\underline{U}_{R\wedge}\underline{B}$ convection electric field, where $\underline{U}_R \approx \underline{V}_e \approx \underline{V}_p$ and hence moving transverse to the direction of the local flow $\underline{V}_p$, rather than, for instance, being snowploughed downstream in the direction of the oncoming flow $\underline{V}_p$. Examples of both these types of behavior can be seen in the results presented in the previous section. From our discussion of (9), the consequence of mass loading the proton flow upstream of the release in this way is simply to deflect the protons locally via a $\underline{U}_{\alpha\wedge}\underline{B}$ directed convection electric field. This of course neglects the possibility of momentum transfer in this upstream region due to ion streaming instabilities, which has been examined by Papadopoulos et al. [1987] and, for the later stages in the picked up release ion motion, by Winske et al. [1985]. Hence the direction of our one-dimensional study, which is just the direction of the oncoming proton flow close to the dense region of the release cloud and diamagnetic cavity, may lie in the plane of Figure 7 along a direction which is at an angle β to the ambient solar wind direction. Since the magnitude of β depends upon the amount of momentum

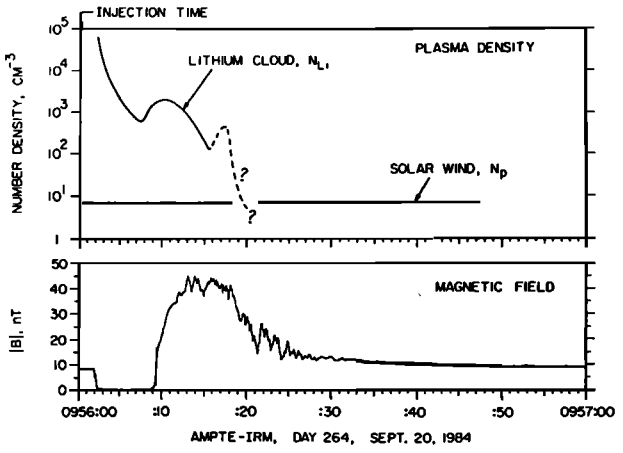

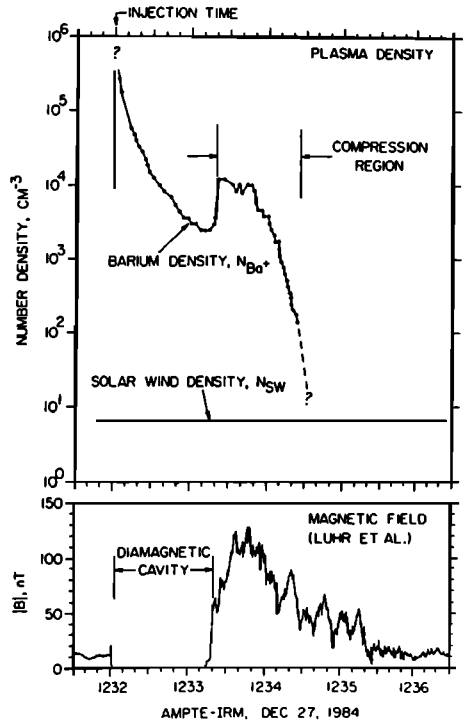

Fig. 8. Release ion number density (obtained from measurements of the plasma frequency) and the magnetic field magnitude plotted versus time, for the lithium release of September 20, 1984, and the barium release of December 27, 1984. Both plots are of measurements made at the IRM and are reproduced from Gurnett et al., [1986a, b]. The magnetic field at the IRM is first reduced to zero at the time of the releases as the diamagnetic cavity forms. The release ion density then falls away due to expansion of the ion cloud, but is then enhanced, its peak preceding the arrival of that of the magnetic field, consistent with the simulation results discussed in the text.

extraction 'upstream', and hence upon the time dependent mass loading in this region, it is difficult to estimate it accurately analytically.

The results of our one-dimensional simulation are shown schematically in the figure. The situation is shown for a time after which the snowplough configuration has evolved. The density spike associated with the snowplough is denoted by the hatched region, upstream of which the field is compressed. At the upstream edge of this field compression region (dashed line) is the upstream potential jump which slows and in some cases reflects the oncoming protons. Release ions created upstream of the snowplough fields in this region are also accelerated further upstream by this potential. Downstream, that is, inside the cavity, the protons emerge from the snowplough fields along with the fast release ion population (that was accelerated by the overshoot in the potential), transverse momentum being conserved between these two species. This fast release ion population may finally emerge from the downstream side of the release cloud, forming a taillike structure.

We can now compare this picture with the overall behavior seen during the AMPTE releases. As the snowplough density spike of release ions and associated field structures move toward the release ion center, they will ultimately sweep over the IRM location. The IRM measurements of magnetic field magnitude and number density (obtained from measurements of the electron plasma frequency) as a function of time, for both a lithium and a barium solar wind release are shown in Figure 8 (reproduced from Gurnett et al. [1986a, b]). In both cases the signatures are similar, quantities differing only in their absolute magnitudes. Looking first at the magnetic field, we see that the time of each release is clearly identified by the rapid suppression of the field to zero as the diamagnetic cavity forms, the subsequent increase in the field to its maximum value marking the time at which the cavity edge moves over the IRM. The density seen at the IRM first decreases due, presumably, to expansion of the release ion cloud and subsequently increases to a peak which is encountered by the IRM just as the magnetic field begins to increase. This peak in density would correspond to the snowploughed release ion population seen in the numerical results presented here and hence would be expected to arrive at the IRM just prior to the peak in the magnetic field, as can be seen to be the case. Later in time on the plot, corresponding to locations further upstream in our simulation, the magnetic field falls away fairly rapidly. This region would correspond to the upstream potential plateau found in the simulation results.

At the first major dip in $|\underline{B}|$, corresponding to the upstream potential jump in our simulation, an intense burst of electrostatic noise is seen at the IRM, extending further upstream where the magnetic field is still disturbed. This disturbed upstream region corresponds to a region in our results where backstreaming protons and release ions interact with the oncoming solar wind population, resulting in increased noise in the electric field. The one-dimensional hybrid code here, however, has been chosen principally to investigate ion kinetic behavior and is therefore sufficiently restrictive to prevent detailed comparisons between our results and the wave data.

A problem which is raised by these, and earlier, simulations (i.e., those of Lui et al.) is that no clear observation has been made of the backstreaming protons by the IRM as it moves through the disturbed field region, at least in the case of the lithium releases [Paschmann et al., 1986]. The electric field intensities detected by the wave instrument, although substantial, appear on initial consideration to be insufficient to scatter the reflecting proton beam sufficiently to render it unobservable. A further possibility for resolving this problem is that, in the case of lithium, the reflected proton beam was directed at the IRM over too brief an interval of time to be detected. The IRM ion instrument

does not in general have contiguous coverage in energy and angle [Paschmann et al., 1985], so that in order to remain undetected, the reflected protons would need to be directed at the IRM for ~ 2 s or less, depending upon the polar angle that their trajectories subtend to the IRM spin axis (W. Baumjohann, private communication, 1987). Since in the simple one-dimensional study employed here we have not been able to determine the detailed global motion of the upstream boundary (C) that effectively acts as a source for the reflected proton population, we cannot at present show whether or not the simulation results are in contradiction with the observations in this respect.

It is interesting to note from Figure 8 and from Luhr et al. [1986a] that the maximum field compression in the case of the lithium releases is very close to that found here (i.e., ~ 50 nT, or ~ 5 times the ambient value), but that for the case of the barium releases [Luhr et al., 1986b] the field is enhanced more strongly (by a factor of ~ 12 times the ambient value). We hope to elucidate the detailed dependence of the magnetic field behavior on the various parameters in a future publication.

A requirement of the snowplough structure here is a population of heated electrons located at the cavity edge, just inside of the field compression region in order to provide the gradient in P_e. Evidence of heated electrons in this region [e.g. Paschmann et al., 1986], along with wave noise at the cavity edge [Gurnett et al., 1986a, b] has indeed been found in the release data, although of course our resistive model can only at best mimic the expected bulk electron behavior.

A further indication of the gross behavior of the release cloud is given by the ground based optical measurements that are available for the barium releases [Valenzuela et al., 1986]. Briefly, these images reveal that subsequent to the time that the magnetic field returns to the IRM location, the bulk of the release ions are seen to initially move en masse in a direction close to $+\underline{V}_{sw}\wedge\underline{B}$, transverse to the ambient solar wind direction, before finally being transported in the $-\underline{V}_{sw}$ direction. In our simple picture of Figure 7 this would correspond to the snowplough moving through the cavity in the direction of the local disturbed oncoming flow which has been deflected by momentum extraction upstream. We have not demonstrated in this brief discussion here that there will be the required deflection β to account for this observed motion of the release cloud. However, we note that the direction of draping of the external field over the barium release cloud, which would be produced by a skew in the oncoming flow, is consistent with its ultimate transverse displacement [Dunlop et al., 1987]. The observed bulk flow itself [Haerendel et al., 1986] in this region appears to be deflected in the direction of the skew in the field (i.e., in the direction of transverse displacement of the release ion cloud). Interpretation of measurements of the ion bulk flow, and indeed the detailed ion spectra themselves, made of the release events is, however, difficult as the plasma instruments on board the UKS and IRM cannot distinguish between ion species of different masses. It is therefore beyond the scope of this paper to attempt to determine the flow displacement angle β from the release ion data.

Our results further predict the presence of a fast moving tail of release ions, moving approximately along (although slightly displaced from) the longitudinal ($\hat{x}$) direction of our simulation (see Figure 7) and hence here approximately in the direction of motion of the snowploughed bulk of the release ions. This population can clearly be identified in the images taken by Mendillo and Baumgardner (reported by Valenzuela et al., [1986]) of the first barium release. At much lower intensities, other features are observed, such as a release ion tail directed in the ambient solar wind flow direction, on a much larger scale than the features discussed above, and a barium ion population streaming in the opposite direction to the predominant release ion motion (i.e., opposite to the snowploughed population in the scenario of Figure 7). Here we simply note that, provided the deflection β of the oncoming flow in Figure 7 is sufficiently large, the forces required to accelerate release ion populations in these directions clearly exist. Release ions created outside the snowplough can be accelerated in the opposite direction to the snowplough motion by interacting with the same potential jump which acts to slow down the oncoming protons, an example of which is shown in the simulation results presented here. Futhermore, these ions will be subjected to a transverse acceleration in the local $-\underline{V}\wedge\underline{B}$ convection electric field, which, if the local flow direction has become distorted to be transverse to the ambient flow direction, will point along the direction of the ambient flow. Further analysis is required in order to determine whether or not this description can account quantitatively for the actual observations.

One important result from our simulations is that no release ions succeed in traversing the quasi-steady boundary, to move from the diamagnetic cavity to the upstream region (or vice versa). Thus the momentum exchange responsible for the motion of the release ion cloud as a whole, and the formation of fast ion tail structures, transverse to the direction of the ambient flow, must, if proceeding via the scenario of Figure 7, be achieved by ions which at the time of ionization were outside the snowplough-forming region. Therefore in the description suggested above, the required momentum transfer to the release ion cloud is not achieved via an "extraction" mechanism as envisaged by other authors [e.g., Haerendel et al., 1986; Cheng, 1987]. Even if an extraction process is possible due to other aspects neglected here (three-dimensional structure, microinstabilities, etc.) the recoil momentum lost by these particles as they accelerate essentially along the local convection electric field is only transferred to the bulk of the release ions indirectly via the accompanying solar wind deflection β, as sketched in Figure 7. An alternative suggestion (Papadopoulos and Lui, 1986] is that the transverse motion of the ion cloud is due to an $\underline{E}\wedge\underline{B}$ drift of the bulk of the release ions that originally were associated with the diamagnetic cavity, in the enhanced magnetic fields upstream. We have, however, seen that the corresponding population in our one-dimensional simulation (i.e., the snowplough population) does not drift significantly in the direction transverse to the oncoming flow, the only release ions to do so being those that were ionized upstream of the snowplough field region as discussed above. In conclusion, then, we find that the investigation conducted here using a simplified geometry and release density profile, in order to establish the way in which momentum can be transferred locally between the two ion species, has produced results which also have significant implications for the overall global behavior observed for the AMPTE releases.

5. Summary

We have presented results of a one-dimensional hybrid simulation of the boundary region that exists between the dense release plasma and its associated diamagnetic cavity, and the oncoming solar wind flow and field. The chosen model (i.e., kinetic ions, massless fluid electrons) and simplified initial conditions have allowed us

to focus in detail on the way in which momentum transfer proceeds between the two ion species.

Our main findings are as follows:

1. A quasi-steady field and plasma structure evolves which allows momentum transfer to take place on scales which are smaller than the gyroscales of both ion species. Both electron and magnetic pressures act along the direction of incident flow to accelerate the release ions en masse in a snowplough type process. The release ion density spike is accelerated downstream of the magnetic field peak, consistent with observations.

2. Transverse to the oncoming flow direction, momentum transfer is solely "$\underline{V}\wedge\underline{B}$" directed and is only found to be significant upstream of the release ion snowplough population.

3. From simple considerations an analytical estimate of the snowplough speed has been obtained which is in excellent agreement with the simulation results. Ultimately, this should allow scaling of the results presented here to the parameters of the actual AMPTE releases.

4. In the previous section, we have discussed details of the simulation results in the context of the three-dimensional geometry of the actual releases. Although our study is of a simplified release ion density profile and in one dimension, the resolution that these simplifications have allowed reveals details which, in the context of this discussion, have clear parallels in the data. In particular, within the qualitative framework presented here the simulation results are consistent with the observed transverse displacement of the barium release ion clouds, the ion taillike features that are observed to be directed transverse to the ambient flow, the $\underline{V}\wedge\underline{B}$ deflection of the oncoming protons, the enhancement and direction of the skew in the draped magnetic field, and the presence of heated electrons inside the cavity.

Appendix

In this study we assumed that both quasi-neutrality and the massless electron approximation are consistent with the scales of the physical processes that have been discussed. Here we investigate the validity of these approximations in the light of the results given in the text.

Quasi-Neutrality

We can obtain the difference in the plasma densities from

$$\nabla \cdot \underline{E} = -\frac{d^2\varphi}{dx^2} = \frac{\rho}{\epsilon_o} \tag{A1}$$

which is not required in the hybrid calculation itself. If we now consider ions accelerated to energy ϵ (in electron volts) by a potential jump $\Delta\varphi$ across a small distance ΔL, then

$$\frac{n_i - n_e}{n} \ll 1 \quad \text{implies} \quad \frac{\epsilon_o\,\epsilon}{n\,\Delta L^2 q} \ll 1 \tag{A2}$$

We have seen that the largest gradient in E_x is that which decelerates the protons. Hence the proton slowing-down scale (to rest) must satisfy

$$\Delta L \gg \left[\frac{\epsilon_o \epsilon_p}{nq}\right]^{\frac{1}{2}} = \frac{V_p}{\sqrt{2}\,\omega_p} = 0.12 \text{ km} \tag{A3}$$

for typical solar wind values. This then places a lower limit on the resolution of the grid for consistency (rather than the Debye length which is typically $\sim$ 7.4 m in the solar wind) and is well satisfied by our simulations.

Massless Electron Approximation

We shall briefly compare the magnitudes of the inertial and remaining terms of the electron fluid momentum equation,

$$nm_e\left[\frac{d\underline{V}_e}{dt} + V_{ex}\frac{d\underline{V}_e}{dx}\right] = -en\left[\underline{E} + \underline{V}_e\wedge\underline{B}\right] - \frac{dP_e}{dx}\,\hat{x} - ne\eta\underline{J} \tag{A4}$$

in order to find the conditions under which the inertial terms may be neglected. Looking first at the $\hat{x}$ component of (A4) gives

$$n\,m_e\left[\frac{V_{ix}}{T} + \frac{V_{ix}^2}{L}\right] = -\,n\frac{\epsilon}{L} - \frac{B_z^2}{L\mu_0} - \frac{nT_e}{L} \tag{A5}$$

where we have used $V_{ix} = V_{ex}$, $eE_x.L = \epsilon$, $Jy = nq\,V_{ey}$ and $P_e = nT_e$, and L and T are typical length and timescales.

The condition that the two terms on the left-hand side are negligible compared to each individual term on the right-hand side then gives

$\frac{d\underline{V}_e}{dt}$ term:			$V_{ex}\frac{d\underline{V}_e}{dx}$ term:		
$\frac{\epsilon}{m_i V_{ix}}$	$\gg \frac{T}{L}$	$\gg \frac{m_e}{m_i}$	$\frac{\epsilon}{\epsilon_{ix}}$	$\gg \frac{m_e}{m_i}$	(A6a)
$\frac{V_A^2}{V_{ix}}$	$\gg \frac{T}{L}$	$\gg \frac{m_e}{m_i}$	$\frac{V_A^2}{V_{ix}^2}$	$\gg \frac{m_e}{m_i}$	(A6b)
$\frac{T_e}{m_i V_{ix}}$	$\gg \frac{T}{L}$	$\gg \frac{m_e}{m_i}$	$\frac{T_e}{\epsilon_{ix}}$	$\gg \frac{m_e}{m_i}$	(A6c)

where ϵ_{ix} is just the kinetic energy of this component of the ion motion $m_i V^2_{ix}$. Similarly, the $\hat{y}$ component of (A4):

$$m_e\left[\frac{B_z}{\mu_0 LneT} + \frac{V_{ix}\,B_z}{L^2\mu_0 ne}\right] = -e\,E_y + e\,V_{ix}B_z - \frac{e\eta B_z}{\mu_0 L} \tag{A7}$$

gives

$\frac{d\underline{V}_e}{dt}$ term:			$V_{ex}\frac{d\underline{V}_e}{dx}$ term:		
$\frac{c^2}{\omega_{pe}^2}\frac{1}{L}$	$\ll \frac{E_y T}{B_z}$		$\frac{c^2}{\omega_{pe}^2}\frac{1}{L^2}$	$\ll \frac{E_y}{B_z}\frac{1}{V_{ix}}$	(A8a)

$$\frac{c^2}{\omega_{pe}^2}\frac{1}{L} \ll V_{ix}\frac{T}{} \qquad \frac{c}{\omega_{pe}} \ll L \qquad \text{(A8b)}$$

$$\frac{c^2}{\omega_{pe}^2}\frac{1}{L} \ll \frac{\eta}{\mu_o}\frac{T}{L} = L_{\eta c} \qquad \frac{c^2}{\omega_{pe}^2}\frac{1}{L^2} \ll \frac{\eta}{\mu_o V_{ix}} = \frac{L_{\eta i}}{L} \qquad \text{(A8c)}$$

where L_η is the resistive scale length, over which the magnetic Reynolds number $R_m \approx 1$.

For the massless electron approximation to hold, so that each term on the left-hand side is always negligible in comparison with some combination of terms on the right-hand side of (A4), we require at least one inequality out of each of the columns of three in (A6) and (A8) to be satisfied. We can now consider whether this is generally true for the particle, field, and plasma parameters discussed in the text. In this case the characteristic velocity L/T is just the plasma bulk speed V_{ix}, and the inequalities in the left- and right-hand columns become identical. We then find that the first inequality in (A6) is always satisfied at the potential jumps found in the simulation, since these are just sufficient to accelerate or decelerate the ions and $\epsilon \approx \epsilon_{ix}$. The second inequality is satisfied throughout the undisturbed solar wind, where $M_A \simeq 5$, and of course in the field pileup region where the total bulk flow speed is reduced, breaking down only in the field zero region where $V_A \to 0$. On the other hand, the third inequality is always well satisfied in the region where the release ions dominate, only becoming most suspect in the undisturbed solar wind. Looking at the inequalities (A8), it is clear that the massless electron approximation will be satisfied provided $c/\omega_{pe} \ll L$, imposing a lower limit on the spatial resolution of the simulation. Thus the neglect of electron inertia in both $\hat{x}$ and $\hat{y}$ electron fluid equations is well satisfied in our simulations.

Acknowledgments. The authors would like to thank M. W. Dunlop for discussions concerning the AMPTE release data and D. Burgess for providing the forerunner of the code used in this work. This work was supported by the U.K. Science and Engineering Research Council.

The Editor thanks B. D. Scott and another referee for their assistance in evaluating this paper.

References

Brecht, S. H., and V. A. Thomas, Three- dimensional simulation of an active magnetospheric release, J.Geophys. Res., 92, 2289, 1987.

Chapman, S. C., and M. W. Dunlop, Ordering of momentum transfer along $\underline{V}\wedge\underline{B}$ in the AMPTE solar wind releases, J. Geophys. Res., 91, 8051, 1986.

Cheng, A. F., Transverse deflection and dissipation of small plasma beams and clouds in magnetized media, J. Geophys. Res., 92, 55, 1987.

Dunlop, M. W., D. J. Southwood, and W. A. C. Mier-Jedzejowicz, On a magnetic source of southward motion of the AMPTE solar wind barium release of 27th Dec 1984, Planet. Space Sci., in press, 1987.

Gurnett, D. A., T. Z. Ma, R. R. Anderson, O. H. Bauer, G. Haerendel, B. Häusler, G. Paschmann, R. A. Treumann, H. C. Koons, R. Holzworth, and H. Lühr, Analysis and interpretation of the shocklike electrostatic noise observed during the AMPTE solar wind lithium releases, J. Geophys. Res., 91, 1301, 1986a.

Gurnett, D. A., R. R. Anderson, T. Z. Ma, G. Haerendel, G. Paschmann, O. H. Bauer, R. A. Treumann, H. C. Koons, R. H. Kolzworth, and H. Lühr, Waves and electric fields associated with the first AMPTE artificial comet, J. Geophys. Res., 91, 10,013, 1986b.

Haerendel, G., G. Paschmann, W. Baumjohann and C. W. Carlson, Dynamics of the AMPTE artificial comet, Nature, 320, (6064), 720, 1986.

Krall, N. A., and A. W. Trivelpiece, Principles of Plasma Physics, Mc Graw Hill, New York, 1973.

Krimigis, S. M., G. Haerendel, R. W. McEntire, G. Paschmann, and D. A. Bryant, The Active Magnetospheric Particle Tracer Explorers (AMPTE) program, Eos, Trans. AGU, 63, 843, 1982.

Lühr, H., D. J. Southwood, N. Klöcker, M. Acuña, B. Häusler, M. W. Dunlop, W. A. C. Mier-Jedrzejowicz, R. P. Rijnbeek, and M. Six, In situ magnetic field measurements during AMPTE solar wind Li^+ releases, J. Geophys. Res., 91, 1261, 1986a.

Lühr, H., D. J. Southwood, N. Klöcker, M. W. Dunlop, W. A. C. Mier-Jedrzejowicz, R. P. Rijnbeek, M. Six, B. Häusler, and M. Acuña, In situ magnetic field observations of the AMPTE artificial comet, Nature, 320, (6064), 1986b.

Lui, A. T. Y., C. C. Goodrich, A. Menkofsky, and K. Papadopoulos, Early time interaction of lithium ions with the solar wind in the AMPTE mission, J. Geophys. Res., 91, 1333, 1986.

Papadopoulos, K., and A. T. Y. Lui, On the initial motion of artificial comets in the AMPTE releases, Geophys. Res. Lett., 13, 925, 1986.

Papadopoulos, K., J. D. Huba, and A. T. Y. Lui, Collisionless coupling in the AMPTE artificial comet, J. Geophys. Res., 92, 47, 1987.

Paschmann, G., H. Loidl, P. Obermayer, M. Ertl, R. Laborenz, N. Sckopke, W. Baumjohann, C. W. Carlson, and D. W. Curtis, The plasma instrument for the AMPTE IRM, IEEE Trans, Geosci. Remote Sens., GE-23, 2062, 1985.

Paschmann, G., C. W. Carlson, W. Baumjohann, H. Loidl, D. W. Curtis, N. Sckopke, and G. Haerendel, Plasma observations on AMPTE/IRM during the lithium releases in the solar wind, J. Geophys. Res., 91, 1271, 1986.

Valenzuela, A., G. Haerendel, H. Foppl, H. Neuss, E. Rieger, J. Stöcker, O. Bauer, H. Höfner, and J. Loidl, The AMPTE artificial comet experiments, Nature, 320, (6064), 700, 1986.

Winske, D., and M. M. Leroy, Hybrid simulation techniques applied to the earth's bow shock, in Computer Simulations of Space Plasmas - Selected Lectures at First ISSS, edited by H. Matsumoto and T. Sato, p. 568, D. Reidel, Hingham, Mass., 1985.

Winske D., C. S. Wu, Y. Y. Li, Z. Z. Mou, and S. Y. Guo, Coupling of newborn ions to the solar wind by electromagnetic instabilities and their interaction with the bow shock., J. Geophys. Res., 90, 2713, 1985.

S. C. Chapman and S. J. Schwartz, School of Mathematical Sciences, Queen Mary College, Mile End Road, London, E1 4NS, England.

(Received March 30, 1987;
revised June 25, 1987;
accepted June 29, 1987.)